Axo-Axonic Synapses on Descending Neurons in the *Drosophila* Ventral Nerve Cord

Cesar Ceballos[1], Juan Lopez[1], Ty Roachford[1], Daniel Sanchez[1], Sabrina Jara[1], Kelli Robbins[1], Casey Spencer[2], Rodney Murphey[1], Rodrigo FO Pena[1,*]

[1]Department of Biological Sciences, Florida Atlantic University, FL 33458, Jupiter, Florida, USA

[2]Harriet Wilkes Honors College, Florida Atlantic University, Jupiter, FL, 33458, USA

*penar@fau.edu

Abstract

Axo-axonic synapses can veto, amplify, or synchronize spikes, yet their circuit-scale logic is unknown. Using the complete electron-microscopy connectome of the adult male Drosophila ventral nerve cord (MANC v1.2.1), we charted every axo-axonic input onto the 1,314 descending neurons that carry brain commands to the body. Only 1.0 % of the 861,591 possible Descending–Descending neuron pairs form such contacts, but when present, synaptic weight grows linearly with partner number regardless of transmitter identity. High-degree neurons integrate the network without forming a rich-club core. Large-scale simulations singled out an octet of ascending neurons (AN08B098) whose axo-axonic input to the Giant Fiber descending neurons (DNp01) predicted modulation of escape control. Immunostaining confirms their cholinergic identity, while optogenetic activation confirmed that this excitatory cohort increases Giant Fiber excitability, validating connectome-derived rules. Our work delivers the first map of axo-axonic wiring and constraints for models of fast motor control.

Keywords: Connectome, Drosophila, Axo-axonic, Giant Fiber escape circuit, Network topology, Electron-microscopy reconstruction, Motor control

Introduction

Neurons communicate through a variety of synaptic motifs. In flies, the canonical arrangement is axo-dendritic, but a second configuration, axo-axonic, can exert unusually powerful control over spike initiation and transmitter release[1,2]. Axo-axonic cells (AACs) in the mammalian cortex can be seen in chandelier cells that inhibit pyramidal axons at their initial segments, whereas in the spinal cord axo-axonic contacts shape locomotor rhythms[1]. Although these examples hint at broad importance, the quantitative wiring logic of axo-axonic synapses remained poorly understood because no complete system had yet been mapped at the necessary synaptic resolution.

Drosophila melanogaster now provides that opportunity through electron-microscopy reconstructions of the entire adult male nerve cord and female brain (MANC[3–5] and FAFB[6]), which are publicly available through the NeuPrint interface[7]. Early graph analyses of the FAFB data revealed rich-club hubs and other mesoscale motifs[6], but systematic exploration of the ventral nerve cord (VNC), the insect analogue of the vertebrate spinal cord, is only beginning. At the heart of the VNC, a pair of descending neurons known as Giant Fibers (GFs) function as command neurons receiving visual input in the brain and driving jump and flight motor neurons[8,9]. These GFs receive a high number of AACs, thus it is only natural to assume a connection AAC to behavior modulation is in place.

Within the VNC, a single class of neurons is ideally positioned for studying axo-axonic wiring and their connection to the GFs. Descending neurons (DNs) have their somata and dendrites in the brain yet project their axons into the VNC[10–13]. Any synapse made onto a DN within the cord is, by definition, axo-axonic. The MANC connectome contains DN, ascending neurons (ANs), intrinsic interneurons (INs) and motor neurons (MNs) offering a comprehensive substrate for network-wide analysis of this motif. Although classic anatomical work suggested that each GF acts largely in isolation, our work using the MANC connectome reveals an unexpectedly rich set of axo-axonic inputs onto the GF axons, including direct contacts from other DNs, ANs, and INs. In the present study we show that the GF receives 97 distinct axo-axonic partners with some offering a crucial role for axo-axonic modulation, i.e., an octet of ascending neurons (AN08B098).

Past light-microscopic surveys catalogued individual DN types and noted scattered DN-to-DN contacts[10], yet the circuit-level role of axo-axonic synapses has remained unexplored. The outstanding issues are their prevalence, partner preference and functional impact on fast behavior. Specifically, it is unknown (i) how frequently axo-axonic connections occur among the 861,591 possible DN pairs, (ii) whether DNs connect preferentially to neurons of their own morphological type or equally across types, and (iii) whether such a sparse motif can nevertheless mediate rapid, system-wide control required for escape. We tackle these questions by mining the complete electron-microscopy connectome of the adult male ventral nerve cord (MANC). Our analysis (i) enumerates every axo-axonic input onto all 1,314 DNs, (ii) dissects morphology relationship to DN connectivity, (iii) shows that the DN network is small-world but not rich-club, partitioned into

thirteen functional communities, (iv) uses large-scale leaky integrate-and-fire simulations to predict which highly connected AACs modulate the Giant Fiber escape pathway, and (v) confirms those predictions with targeted optogenetic activation *in vivo*.

Our results provide the first system-level blueprint of axo-axonic wiring in an adult nervous system and suggest general design principles for descending motor control that may extend beyond insects. They also illustrate the functional power of the sparse axo-axonic network described below and place the GFs at the center of a distributed control system rather than a simple linear reflex arc.

Results

Global Distribution of Axo-Axonic Inputs to Descending Neurons.

To uncover the prevalence of axo-axonic connections between DNs in the VNC, we used the MANC dataset available through the NeuPrint+ interface and API[14–16]. Figure 1*A-C* shows morphological reconstructions of some exemplary DNs of interest from Neuroglancer: DNp01 (GFs, black dot), DNd03 (blue dot), and DNg02 (red dot, Fig. 1*A-C*). For each neuron, Neuroglancer overlays the 3D-EM reconstruction on the VNC volume. The GFs, whose axon is nearly unbranched (green or blue), receive one of the highest numbers of axo-axonic inputs (n=97) in the data set. DNd03 is a highly arborized neuron with a similarly large input count (n=160), while DNg02 has less arborization but similar axo-axonic inputs (n=110). Interestingly, all three share similar synaptic strength despite differences in arborization (DNp01 2352, DNd03 2364, DNg02 1751; Fig. 1*H*). Neuroglancer presents transmission-EM micrographs at 500 nm resolution taken from MANC; presynaptic active zones are marked by magenta dots, postsynaptic densities by cyan dots, and partner axons are pseudo-colored to match the 3-D rendering (Fig. 1*D-F*).

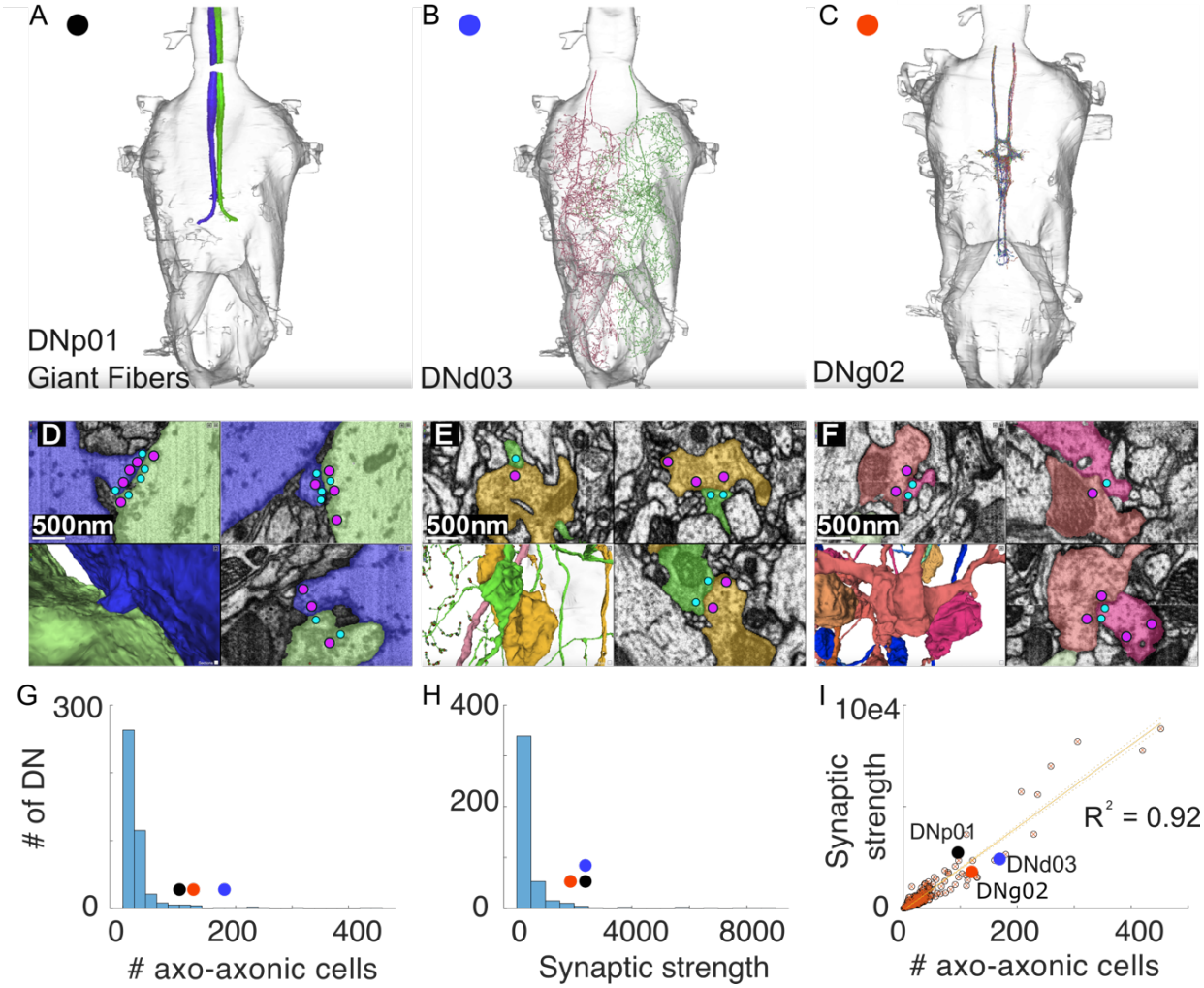

Figure 1. Descending neurons (DNs) and their axo-axonic inputs in the VNC. *(A)*-(*C*) Exemplary Neuroglancer reconstructions of DNs of interest. (*D*)-(*F*) EM images of axo-axonic connections the three reconstructions make. (*D*) shows DNp01 to DNp01 connectivity, (*E*) shows DNd03 connectivity with DNp42 (yellow), and *(F*) shows DNg02 to DNg02 connectivity. Red circles identify the locations of presynaptic T-bars; blue circles show postsynaptic densities. Circles were enlarged for visibility. (*G*) Histogram of the number of axo-axonic neurons innervating one DN. Presynaptic neurons can be DN, AN, or IN. (*H*) Histogram of the cumulative strength of the synaptic connections for each DN. Presynaptic neurons can be DN, AN, or IN. (*I*) Scatter plot and linear regression of the number of axo-axonic neurons vs their connection strength. $R^2 = 0.92$ and $p < 0.001$.

We quantified the distribution of axo-axonic connections made onto DNs reported by MANC. Figure 1*G* reveals a highly skewed distribution of partner count; the median DN is innervated by a single presynaptic neuron (inter-quartile range 1–3), and 11% of DNs receive input from only one cell with a connection weight of six or greater. A small set of outliers, however, attracts hundreds of partners, including DNp01 (GFs) with 97 distinct axo-axonic inputs. Strikingly, the GFs receive these connections despite possessing one of the simplest axonal arbors in the dataset (Fig. 1*A*). All other DNs have more branched and complex axonal trees, which we expect to explain their degree of innervation. Total input strength follows a similar heavy-tailed pattern (Fig. 1*H*). The modal DN receives fewer than 20 synapses, whereas the GF is again among the top of the list in terms of individual contacts. Across the population, partner count and cumulative weight are tightly coupled (Pearson $r = 0.96$, $p < 0.001$; Fig. 1*I*), indicating that neurons that recruit many partners also receive proportionally stronger innervation. Together, the findings identified the distribution of axo-axonic connections made with DNs in the VNC. We confirm that the synapses quantified in the graph analysis correspond to active zones and illustrate how neurons with very different morphologies can converge on similar axo-axonic input profiles.

Using these findings, we then explore that anatomical complexity is a strong, though not perfect, predictor of synaptic weight for axo-axonic inputs onto DNs (Fig. 2). Representative reconstructions illustrate the general pattern: neurons with short, unbranched axons receive few contacts, those with intermediate arborization receive proportionately more, and highly branched cells accumulate the greatest axo-axonic weight (Fig. 2*A*-*C*). A kernel density estimation (KDE) plot of all 1,314 DNs reinforces this observation, showing a diagonal ridge in which increasing cable length accompanies increasing total input weight (Fig. 2*F*). Linear, quadratic, and symbolic regressions all yield significant positive slopes, confirming a monotonic relationship (Fig. 2*G*). However, the shallow gradient and the presence of two striking outliers, a long axon with sparse innervation and a short axon with dense innervation, indicate that branch length alone does not determine synaptic investment (Fig. 2*D*-*E*). Thus, we find a presynaptic neuron's morphology sets a broad preferential expectation for how much modulation a partner DN receives, but additional cell-type-specific factors must refine the final allocation of axo-axonic synapses.

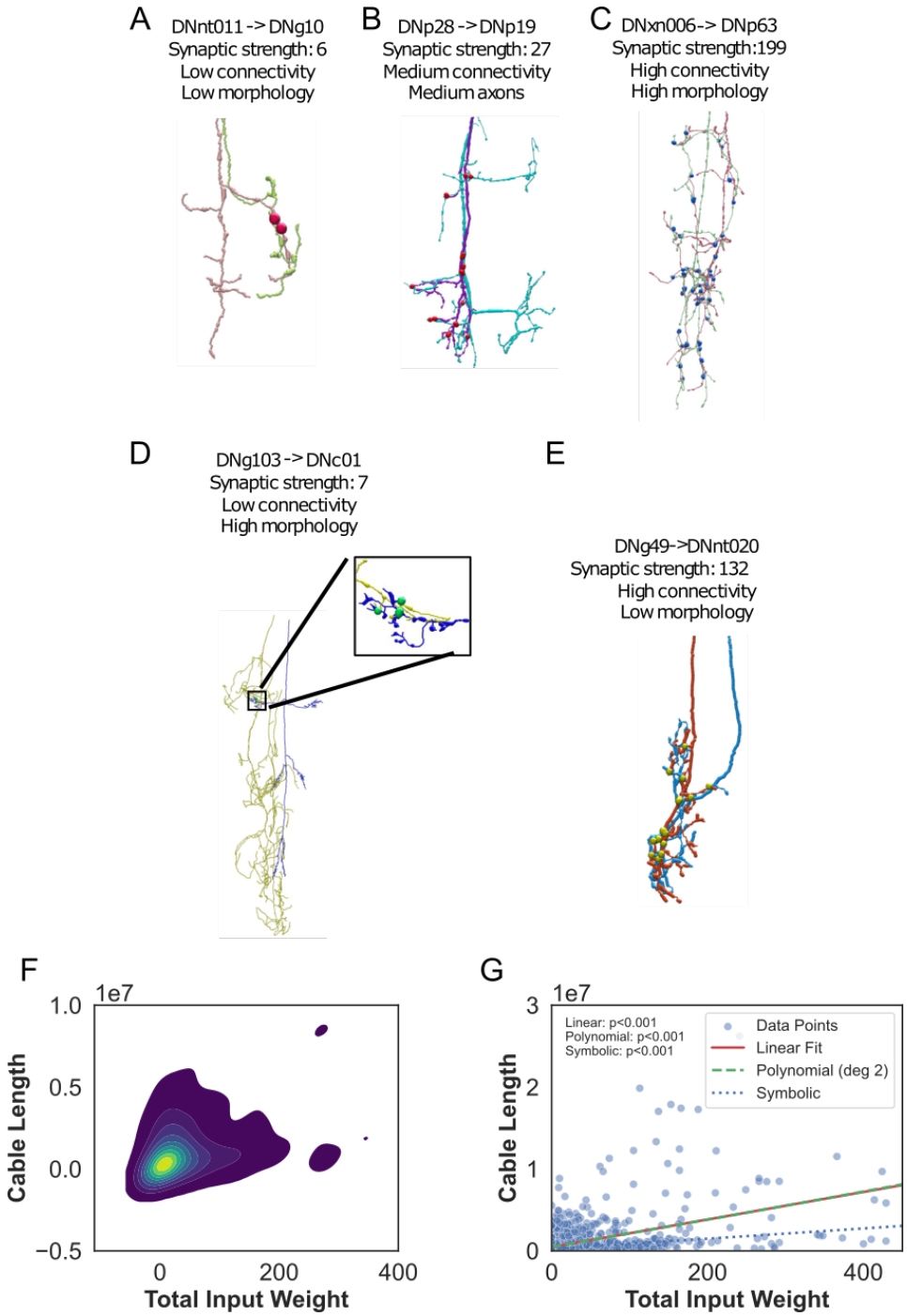

Figure 2. Analysis of morphology and synaptic strength between DN-to-DN axo-axonic connections. (*A*-*E*) Examples of DN: (*A*) low connectivity and low morphology, (*B*) medium connectivity and medium morphology, (*C*) high connectivity and high morphology. But also, (*D*) low connectivity and high morphology, and (*E*) high connectivity and low morphology. These neurons agree with the bulk of the data, where there is a linear correlation between morphology and synaptic strength. Also, neurons at the bottom: (*D*) low connectivity and high morphology, and (*E*) high connectivity and low morphology, are outliers. Dots indicate synapse locations. *F*) Kernel density estimation (KDE) of the scatter data of total input weight vs cable length, *G*) Scatter plot of total input weight vs cable length and the corresponding linear regression, polynomial regression of a quadratic function, and symbolic regression.

Further exploration revealed a unique feature of connectivity. In the nervous system, neurons will often target several downstream partners to form synapses with (Fig. 3*B*). We found and labeled certain neurons, like those of type IN21A026, as single-target neurons when more than ~10% of their reported number of their connections target a single neuron, or neuron type with only two members (e.g., a bilateral pair). Importantly, we identified several single-target axo-axonic connections (Fig. 3*A*) to DNs. Among them, DNp01 is the neuron type that receives the highest number of single-target AACs (n=10; Fig. 3*C*). Among these 10 neurons, five belong to the AN08B098 type, and the remaining are labeled as "unknown".

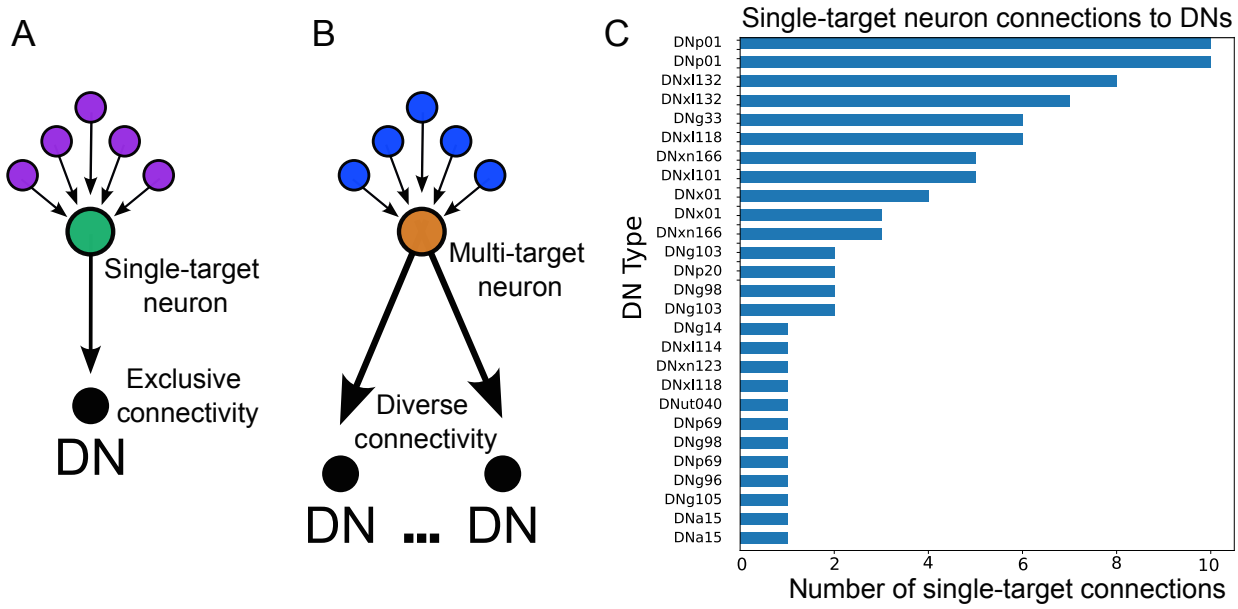

Figure 3. Neurons that provide exclusive axo-axonic connections to DNs. (*A*) Sketch of single-target vs (*B*) multi-target neuron. Single-target neurons project the overwhelming majority, if not all, of their outgoing connections to a single DN. (*C*) Number of exclusive neurons per DN. The Giant Fibers (DNp01) are among a small population of DNs that receive 10 single-target connections, i.e., there are about 10 neurons that innervate DNp01 exclusively.

Compared with other highly connected DNs, the GFs attain an equivalent synaptic strength with a simple morphology, further demonstrating how morphological complexity alone does not predict axo-axonic input. These results identify the GFs as exceptional hubs for axo-axonic modulation due to their significant connectivity despite their relatively simple morphology compared to other highly connected DNs. However, these findings also raise several new questions: Which explicit AAC populations account for the GF's unusually dense axo-axonic input? How do these contacts alter GF excitability? Is the GF an outlier, or do similar axo-axonic motifs govern other rapid motor pathways in the fly? We address these questions by investigating the strongest single-target AAC population presynaptic to the GFs, the AN08B098 type neurons.

Sparse yet Globally Connected Axo-Axonic Network among Descending Neurons.

To study how DNs communicate with other DNs through axons, we extracted every DN-to-DN contact from the updated MANC dataset. The resulting adjacency matrix is strikingly sparse: only about 1% of the possible ordered pairs carry even a single synapse (Fig. 4*A*). Moreover, partner choice is not random: homotypic pairs (same DN type) and heterotypic pairs (different types) show distinct transmitter profiles, as shown for acetylcholine, GABA, and glutamate, implying that neurotransmitter identity contributes to the selectivity of these long-range axo-axonic contacts (Fig. 4*D*). In homotypic DN connections, ~90% of the connections are cholinergic (excitatory), while heterotypic DN connections are ~60% cholinergic [the remaining are GABA/glutamate (inhibitory)]. This suggests that AACs between DNs, while rare, are predominantly excitatory. connections.

We next asked whether the same wiring principle applies to non-descending inputs, namely ascending neurons (ANs) and intrinsic interneurons (INs). Repeating the analysis with ANs and INs as presynaptic partners to DNs again produced very sparse matrices: about 1.2% of all possible AN-to-DN pairs and 0.7% of the IN-to-DN pairs contain at least one synapse (Fig. 4*B*-*C*). Figure 4*E* shows the neurotransmitter profile for AN-to-DN and IN-to-DN pairs. Both pair profiles were similar, with almost half of the neurons being cholinergic and the other half GABA/glutamate. This suggests that AACs between AN-to-DN and IN-to-DN follow the same rules for neurotransmitter identity as DN-to-DN AACs.

Lastly, we show the distribution of the number of pre-synaptic DN, AN, or IN that project axo-axonic synapses to a post-synaptic DN (Fig. 4*F*-*H* top row) as well as the number of postsynaptic DN that are innervated axo-axonically by the same DN, AN, or IN (Fig. 4*F*-*H* bottom row). The distributions are similar between neuron types, with a decay resembling an exponential (Poisson), where a few neurons are largely connected and a few neurons are not. When we merge all three presynaptic classes into a single connectivity matrix (Fig. 4*J*,) the same pattern from Figure 4*A*-*C* emerges: extreme sparseness combined with global reachability (see dots where our exemplary neurons are located; color scheme as in Fig. 1*A*.). We also highlight the degree of convergence across presynaptic classes and identify connectivity hubs in terms of their total input. Taken together, regardless of presynaptic identity, the findings show that the organization of the network combines stringent partner selectivity with complete coverage of the descending system.

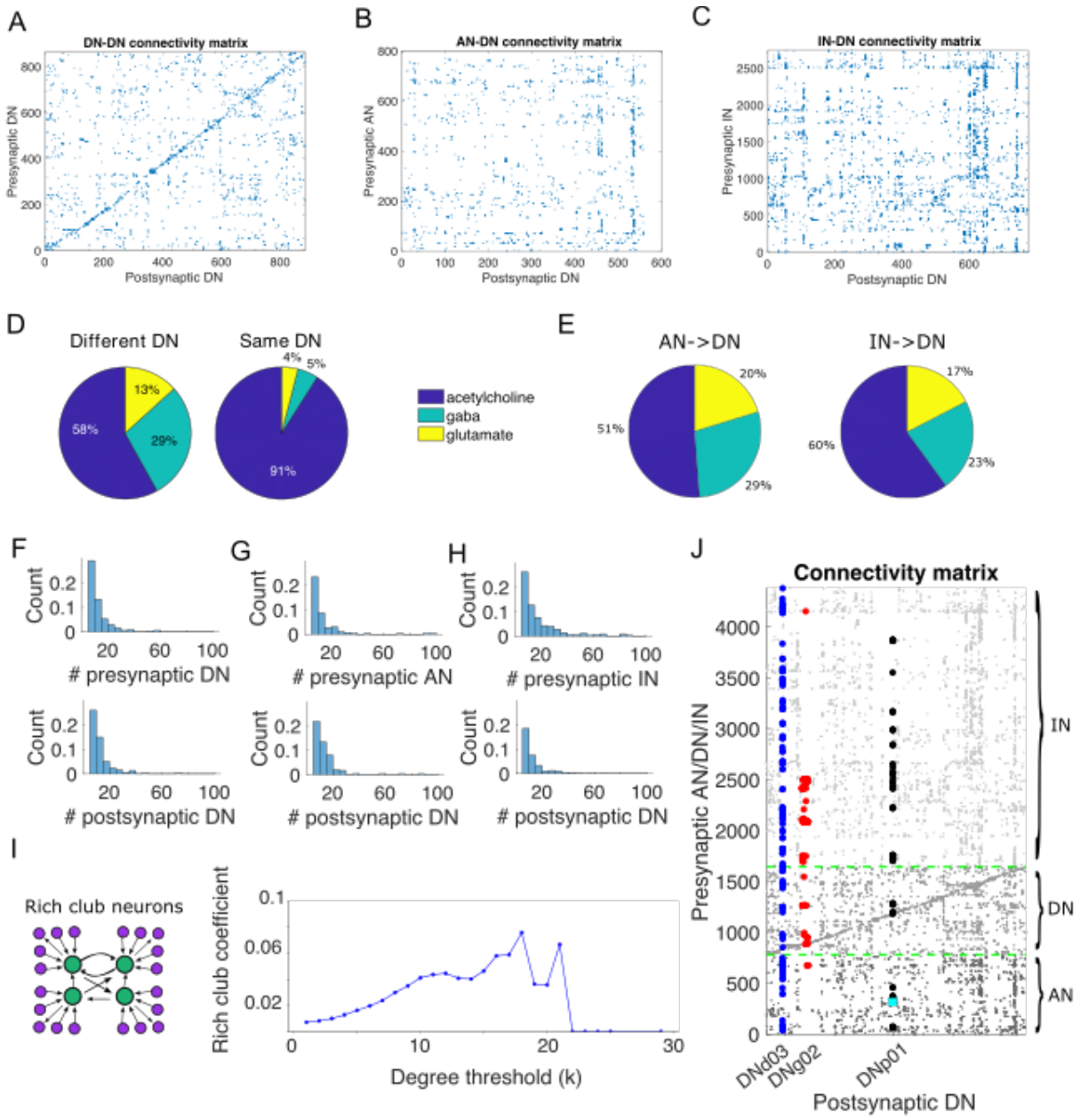

Figure 4. Axo-axonic connectivity is exceedingly sparse yet forms a chemically balanced, globally integrated network among descending, ascending, and intrinsic neurons. (*A*) Connectivity matrix of pairs of DN-to-DN connections. Only 1% of all possible connections were found. This suggests that DN-to-DN axo-axonic connections are extremely rare. (*B*) Connectivity matrix of pairs of AN-to-DN connections. Only 1.2% of all possible connections were found. This suggests that AN-to-DN axo-axonic connections are extremely rare. (*C*) Connectivity matrix of pairs of IN-to-DN connections. Only 0.7% of all possible connections were found. This suggests that IN-to-DN axo-axonic connections are extremely rare. (*D*) Pie chart of predicted neurotransmitter of DN of the different type (left, e.g., DNp01 -> DNp02) and same type (right, e.g., DNp01 ->DNp01) that make pairs of axo-axonic connections. (*E*) Pie chart of predicted neurotransmitter of AN-to-DN and IN-to-DN axo-axonic connections. (*F*) Histograms of the number of presynaptic DN (in-degree) and postsynaptic DN (out-degree) for DN-to-DN pairs. (*G*) Histograms of the number of presynaptic AN and postsynaptic DN for AN-to-DN pairs. (*H*) Histograms of the number of presynaptic IN and postsynaptic DN for IN-to-DN pairs. (*I*) Rich-club analysis of the DN-to-DN axo-axonic network. (*J*) Connectivity matrix of pairs of AN/DN/IN-to-DN connections. Filled circles follow the same color scheme as in Fig.

1*A-C*. Cyan square identifies AN08B098 type neurons. Dashed green lines and gray tones for dots separate ANs, DNs, and INs.

To explore more refined AAC spatial connectivity preferences, we identified global wiring principles and determined whether they are repeated across DNs, ANs, and INs. Figure 5 shows examples of the contralateral axo-axonic connections between DN-to-DN (Fig. 5*A-B*), AN-to-DN (Fig. 5*C-D*), and IN-to-DN (Fig. 5*E-F*). Figure 5*G* shows the percentage of contralateral connections. AACs between contralateral DNs are rare. However, ANs and INs projecting to contralateral DNs are frequent. Interestingly, the neurotransmitter profiles from our earlier findings are preserved regardless of the type of presynaptic neuron, where approximately half of the neurons are cholinergic (excitatory) and the other half is GABAergic/glutamatergic (inhibitory) (Fig. 5*H-J*).

Taken together, these observations paint a consistent picture. Whether the presynaptic axon descends, ascends, or remains intrinsic to the cord, axo-axonic wiring obeys the same two rules: partner selectivity is extremely high, and midline crossing is common only for neurons that share strong reciprocal ties. The result is a VNC in which local subtypes can interact tightly with their mirror images, yet the great majority of neurons remain insulated from direct axo-axonic influence.

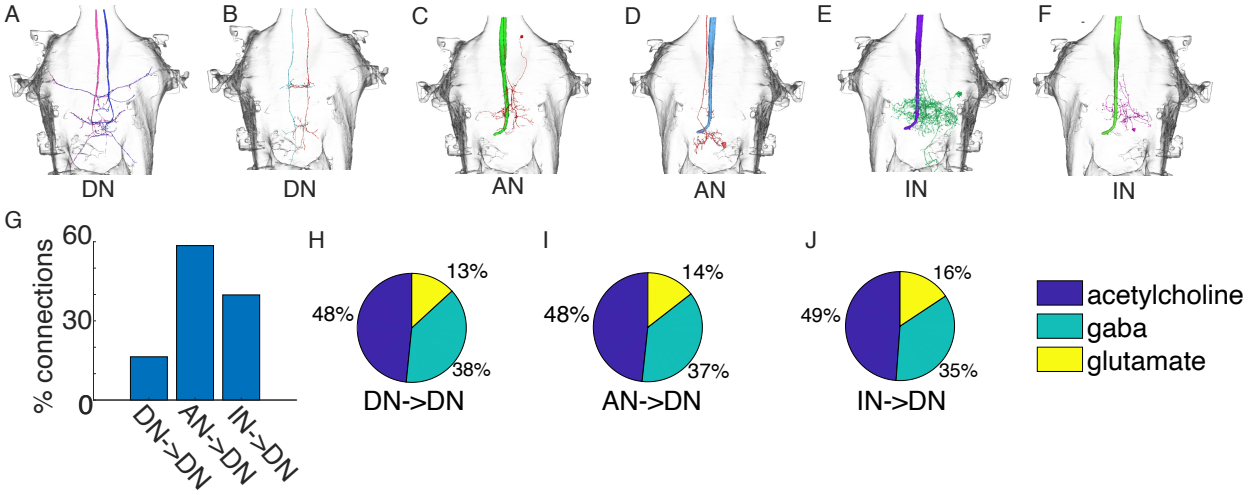

Figure 5. Breakdown of spatial contralateral preference in terms axo-axonic connections. (*A-F*) Examples of each category from DN-to-DN, AN-to-DN, and IN-to-DN. (*G*) Percentage of contralateral connections between DN-to-DN, AN-to-DN and IN-to-DN. (*H-J*) Pie chart of predicted neurotransmitter of DN to contralateral DN, AN to contralateral DN, and IN to contralateral DN of axo-axonic connections.

Graph-Theoretic Architecture of the DN-to-DN Axo-Axonic Network.

We utilized the connectivity matrix we generated as a directed graph to examine how the sparse axo-axonic links between DNs are organized at the system level (Fig. 4*A*). The graph contains 884 nodes and 2,757 edges, giving a density of 0.007. Despite this low density, the average shortest-path length is only 4.03, showing that any two DNs can be reached through a small number of intermediate axonal contacts. The clustering coefficient is likewise low at 0.013, indicating limited local redundancy. Community detection identifies 13 separate modules, consistent with the

functional subdivision of the network. Node degree ranges from 1 to 29 with a mean of 6.24, reflecting a modest hierarchical spread.

The rich-club coefficient Φ(k) measures the density of connections among nodes whose total degree (in-degree + out-degree) equals or exceeds a threshold k. Φ(k) = 1 indicates that the high-degree subgraph is fully connected, whereas Φ(k) = 0 means that those nodes share no edges beyond chance level. The rich-club coefficient in our data peaks at 0.076 for nodes with degree at least 18, so high-degree hubs do not preferentially connect to each other; integration is therefore distributed rather than centralized (Fig. 4*I*). The modest peak value and the absence of a sustained plateau indicate that high-degree DNs do not preferentially interconnect to form a rich club; instead, network integration is distributed rather than hub-dominated.

A slightly positive degree assortativity of 0.029, a measure that suggests tendency of nodes to connect with other nodes in a similar way, suggests a weak tendency for neurons of similar degree to link. Finally, the maximum betweenness centrality of 0.049, a measure that points to how often a node lies on the shortest path between all pair nodes in a network, highlights a small set of bridge neurons that channel information between modules. Together, these metrics portray a network that combines efficient global communication with modular specialization, an architecture well-suited for coordinating diverse motor outputs.

New exclusive axo-axonic modulators of the Giant Fiber escape circuit.

The MANC connectome introduces several novel neuron types to the Giant Fiber escape circuit. To understand and underscore the significance of AAC modulation of the circuit, it is important to know which individual cells can exert a strong, targeted influence on a system such as the GF system[8,9]. As shown in Figure 3, the GFs are among a small population of DNs that receive single-target connections. A focused search within MANC revealed the AN08B098 type neurons, a cluster of 8 pairs of neurons whose axo-axonic output is nearly exclusive and among the strongest to the GFs (Figs. 3-4). These AN08B098 type neurons are predicted to be cholinergic by the MANC connectome.

To test whether the connectome-predicted AN08B098 type neurons truly form chemical AACs with the GFs, we performed a series of experiments. We used split-Gal4 drivers to direct membrane-bound GFP to AN08B098 axons, back-filled the GFs with tetramethyl-rhodamine, and labelled presynaptic active zones with anti-Bruchpilot (nc82). High-resolution confocal stacks revealed discrete GFP-positive boutons that colocalize with Brp puncta on the descending GF tract in the first thoracic neuromere (Fig. 6*A*-*C*), confirming axo-axonic contacts between AN08B098 type neurons and GFs for the first time. Immunostaining for Choline Acetyltransferase (ChAT) showed that AN08B098 somata, as labelled through genetic expression of mCD8::GFP, are ChAT-positive (Fig. 6*D*-*G*), establishing this cohort as likely cholinergic and therefore excitatory.

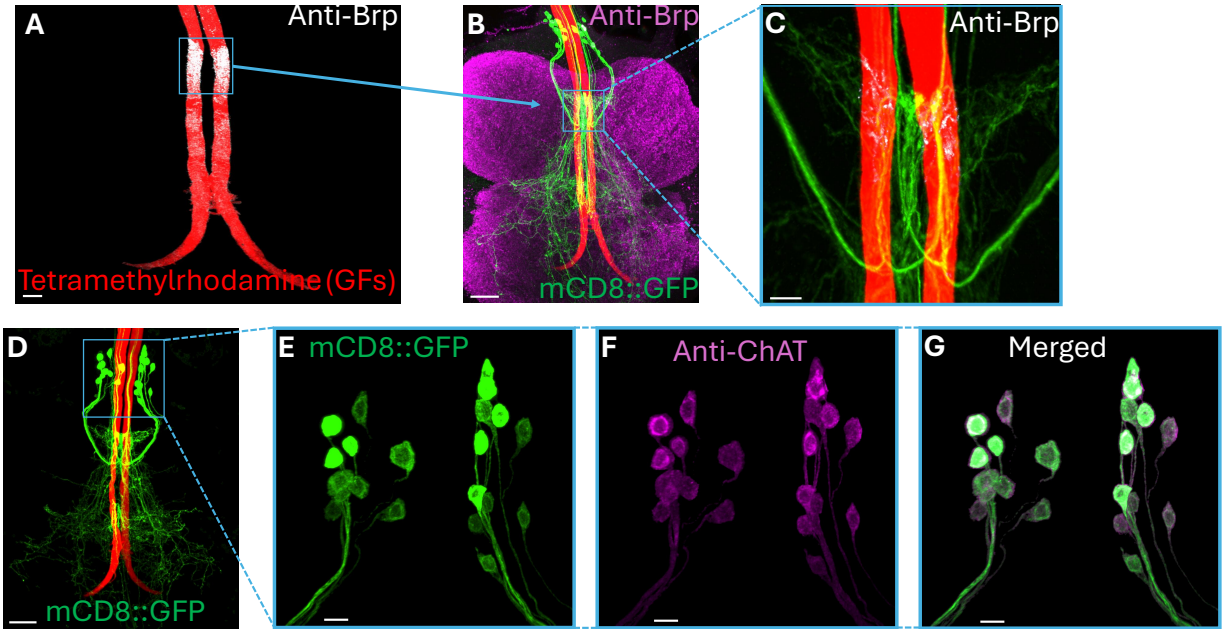

Figure 6. AN08B098 cells make cholinergic axo-axonic synapses on the GFs. (*A*) Immunofluorescence of the presynaptic active zones localized to the GFs. GFs (red) are injected with tetramethylrhodamine and immunolabeled with anti-bruchpilot (Brp). Colocalized GF-Brp is labeled in white. Scale bar represents 10 µm. For each image shown, volume rendering of confocal z-stacks was performed using Imaris v10.2.0. Lookup tables (LUTs) for each channel were manually adjusted for 3D visualization. (*B*) First and second thoracic neuromeres labelled magenta by Anti-Brp. Tetramethylrhodamine labeled GFs, and AN08B098 cells expressing 20XUAS-mCD8::GFP (green). Scale bar represents 20 µm. (*C*) Maximum resolution image (from the boxed area in B) of AN08B098 making an axo-axonic synapse to the GFs. Anti-Brp (white) colocalizes with both AN08B098 and GF rhodamine fluorescence. Scale bar represents 4 µm. (*D*) Separate sample sharing genotype described in B, immunolabeled with GFP and rhodamine. Scale bar represents 20 µm. (*E*) Maximum resolution volume rendering of AN08B098 somas labeled with membrane-bound GFP. Scale bar represents 5 µm. (*F*) same as E, showing masked co-labeled anti-ChAT within AN08B098 somas and terminals. (*G*) Merged images of E and F.

Following this confirmation, we asked whether these AACs can measurably alter GF activity in a simulation of the whole VNC connectome. To test this idea, we stimulated all VNC neurons with a Poisson distribution of excitatory synaptic currents at 30 Hz and 5 nS. Furthermore, one GF was stimulated more strongly at 10 Hz and 40 nS to create a baseline level of excitability (Fig. 7*A,* spikes are shown as large black dots at the bottom of the raster plot). When the eight cholinergic AN08B098 neurons were co-activated, the GF crossed threshold more often, indicating that the axo-axonic inputs are net excitatory (Fig. 7*B*). GF subthreshold voltage histograms quantify the increased excitability (Fig. 7*C*). These simulations highlight a previously unrecognized cohort of axo-axonic synaptic modulation that provides a rapid mechanism for amplifying the escape-circuit output.

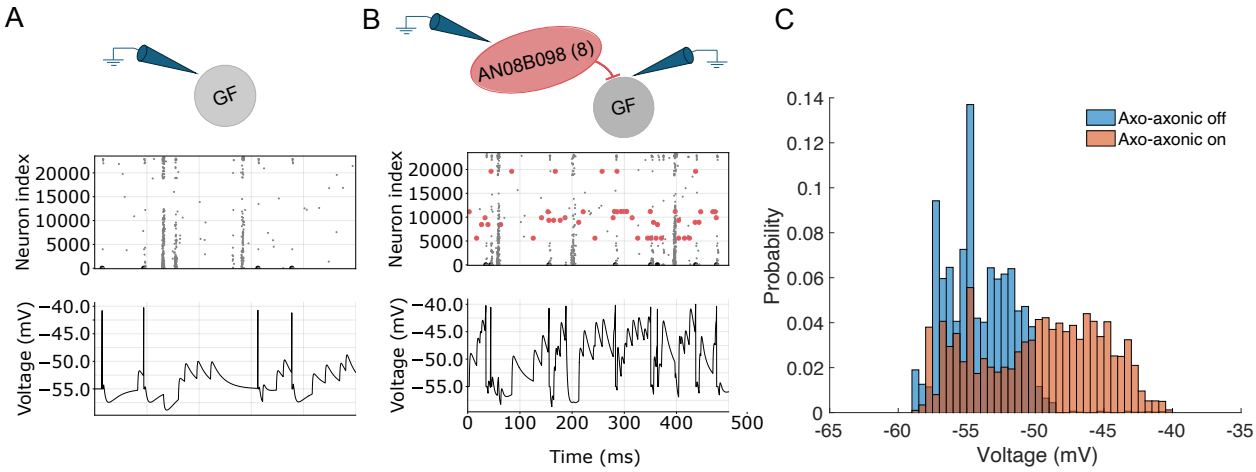

Figure 7. Simulations using the whole VNC network. (*A*) Sketch of the GF and raster plot of all the neurons in the VNC and voltage trace of GF response (spikes are shown as large black dots at the bottom of the raster plot). (*B*) Sketch of the GF being stimulated by the neurons type AN08B098 together with raster plot of all the neurons in the VNC and voltage trace of GF response (GF spikes are shown as large black dots at the bottom of the raster plot and AN08B098 spikes are large red dots). (*C*) Histogram comparison of subthreshold voltages during GF-only and GF+AN08B098 stimulation. The overall excitability of the GF increases when the AN08B098 neurons are activated, leading to higher firing probability for the GF.

Testing connectome predictions *in vivo* via optogenetic stimulation of axo-axonic neurons. To assess the predictions of these connectome simulations, we tested the ideas *in vivo* using classic electrophysiology and optogenetics. Using the split-Gal4 lines that label the AN08B098 neurons mentioned earlier, we verified localized expression of CsChrimson in them and tested their effects on the GF system (Fig. S1).

As a control, we electrically stimulated the GFs at 24 Hz in flies expressing CsChrimson in AN08B098 type neurons and recorded from the jump muscle (TTM) as previously described[17], to confirm that the TTMn was being driven. We then set the electrical stimulation of the GF at 100 Hz and just below threshold. This subthreshold stimulation resulted in no responses seen in the jump muscle (n = 10 GFs, Fig. 8*B*, upper trace and 8*D*). However, when the same preparation was simultaneously illuminated (590 nm), the sub-threshold electrical stimulus elicited responses from jump muscles (Fig. 8*B*, lower trace and 8*E*). A one-way ANOVA found no significant differences between the stimulus pulses for the control group ($p = 0.53$), but there was a significant difference between stimulus pulses for the light group ($p < 0.001$). Post-hoc multiple comparisons found significant differences between stimuli located in the baseline (before light application) and during and after light application. We also found significant differences using a paired t-test when comparing the light vs. the control group for the same stimulus during and after light application, but not before ($p<0.001$ during and after light, $p>0.26$ before light).

We also identified long response latencies and prolonged response occurrences after the light turns off (Fig. 8*B*, *D*, *E*). These features of the response cannot be explained by the time constants of the CsChrimson, which are an order of magnitude shorter than this[18] (~20 ms). Before light

application, the spike probability was low (~20%, black trace, Fig. 8*F*) but during and after light application the spike probability is increased to almost 100% (blue trace, Fig. 8*F*). These results agree with our simulation's predictions that the main effect of the optogenetic activation of the cholinergic axo-axonic neurons (AN08B098) is to increase the excitability of the GF.

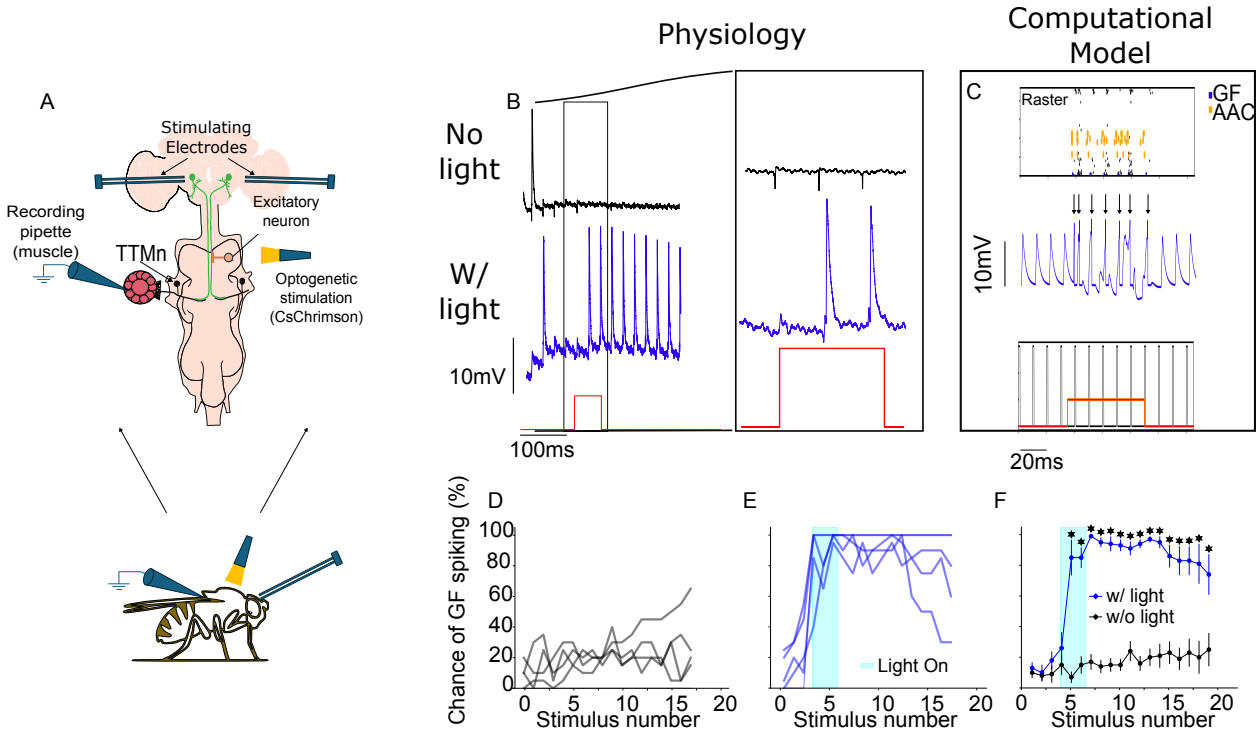

Figure 8. Optogenetic stimulation of excitatory axo-axonic to the Giant Fibers raises the excitability of the escape circuit. (*A*) Sketch of the electrophysiological recordings with optogenetic activation of axo-axonic cells. (*B*) Example of raw traces for control (no light, black) and with light (blue). Square pulse of applied light (bottom). (*C*) Simulation of a computational model of the VNC connectome emulating the experimental results under subthreshold conditions and light stimulation. Note that GF only spikes when the light is applied and is time-locked with the electrical pulses. Action potentials are indicated with arrows. (*D*) Spike probability per fly (n = 5) under no-light conditions. (*E*) Spike probability per fly (n = 5) under light conditions (light was applied during the blue shaded region). (*F*) Average and SEM of spike probability.

We also ran two separate control experiments to confirm that light application has no effect in the absence of the Chrimson expression or function: one with a genotype expressing GFP instead of Chrimson (Fig S2*A*). The second was with the experiment's Chrimson genotype, where we withheld cis-trans-retinal from fly food, thus preventing optogenetic activation of Chrimson (Fig S2*B*). A one-way ANOVA found no significant differences among the stimulus pulses for all the groups ($p = 1$) for the two controls. Post-hoc multiple comparisons found no significant differences between stimuli located in the baseline (before light application), during, and after light. Finally, we found no significant differences using a paired t-test when comparing the light vs. the no-light group for the same stimulus during and after light application, but not before. These control recordings suggest that our results above are a direct consequence of Chrimson light activation.

To confirm the parallel between the simulation and the *in vivo* experiment, we developed a simulation that more closely matched the *in vivo* experiments with optogenetics (Fig. 8*C*). A large-scale network of the VNC made of leaky integrate-and-fire neuron models was used to simulate this experiment. The GF was electrically stimulated just below threshold at 24 Hz. In these simulations, the GF only fires spikes in the presence of the light. Both the simulation and the optogenetic results on the living animal suggest that the AN08B098-to-GF connection is excitatory, consistent with the connectome and chemical prediction that the synapse is cholinergic.

Discussion

By analyzing all 1,314 brain-originating descending neurons, we move beyond scattered descriptions of axo-axonic contacts and derive circuit-level design rules for presynaptic modulation. The quantitative principles that emerged within this work are: (i) extreme sparseness showing that between 0.7 to 1.2% of possible DN-to-DN, AN-to-DN, and IN-to-DN pairs form axo-axonic synapses; (ii) a tight linear relation between synaptic weight and partner multiplicity; and (iii) a small-world architecture that distributes integration rather than concentrating it in a rich-club core. Together, these features constitute a wiring grammar for axo-axonic control in the adult *Drosophila* motor system.

Axo-axonic synapses have been found in the brain of flies[19–21]. Excitatory cholinergic synapses like the ones we investigate have been found in the olfactory system of the fly from Projecting Neurons (PN), making lateral connections with other PN (PN-to-PN connections), the same way we found between DN-to-DN[19]. Another example is found in axo-axonic connections between Olfactory Sensory neurons[21] (i.e., OSN-to-OSN connections). Bristle mechanosensory neurons (BMN) are also shown to be axo-axonically connected[22]. These similarities suggest that axo-axonic connectivity principles might be shared across the VNC and brains of flies, although an investigation of the functional role of AACs has not been done before.

Noticeably, axo-axonic wiring has revealed an extraordinarily selective, yet globally percolating schema, in contrast with, for example, serotonin axo-axonic configuration in the hippocampus, which comprises 30%[23,24] or in the cortex, which comprises 19%[24,25]. In the fly VNC, only ~1 % of the possible DN-to-DN pairs form axo-axonic synapses, an order of magnitude sparser than axo-dendritic contacts in either the MANC or FAFB brain data sets[4,26]. Despite this scarcity, the links suffice to tie every DN into a single strongly connected network, yielding short average path lengths (~4 hops) and thus preserving the ability for any axon to gain rapid, monosynaptic influence over remote peers. This combination of stringent partner choice with network-wide reach resembles presynaptic inhibition motifs in mammalian spinal cord and chandelier-cell control of cortical pyramidal neurons, suggesting convergent architectural solutions across phyla[27,28]. But why are axo-axonic connections so sparse? One possibility is wiring economy: boutons on sister axons consume precious membrane and cytoplasmic resources[29]. Another is developmental lineage. Many high-degree bridge neurons derive from hemilineages that extend across neuromeres[30], hinting that growth-cone timing and Slit-Robo–mediated midline crossing[31] pre-pattern the opportunities for axo-axonic contact. Comparative EM work in other insects and in zebrafish larval spinal cord will clarify whether these archetypes represent a universal motor blueprint.

As previously found, rich clubs with dense interlinking of high-degree hubs are present in the fruit fly connectome[6]. They are also widely present in vertebrates, such as in the cerebral cortex[32,33]. In contrast, the axo-axonic fly DN network showed only a weak, transient rich-club coefficient,

414 arguing that presynaptic modulation in the nerve cord is decentralized. Control must therefore
415 emerge from many mid-degree "broker" neurons with high betweenness rather than from a
416 minority of super-hubs. Such a layout guards against single-point failure and allows different
417 motor modules to be gated independently, consonant with behavioral data showing that flies can
418 blend local reflexes with whole-body maneuvers[34].
419
420 In terms of functional implications, axo-axonic contacts positioned directly on descending axons
421 are ideally placed to veto, amplify, or synchronize commands emanating from the brain before
422 they fan out onto premotor interneurons and motoneurons. Our simulations illustrate this logic:
423 activating a cohort of eight cholinergic AN08B098 type neurons that exclusively target the Giant
424 Fibers (GFs) accelerates their firing. Choline acetyltransferase (ChAT) immunostaining confirms
425 that AN08B098 type neurons are cholinergic, and optogenetic activation of these cells reliably
426 enhances the GF's excitability, confirming the large-scale network of leaky-integrate-and-fire
427 neuron simulations.
428
429 Crucially, however, the GF is not unique; 17 other DNs receive >50 presynaptic partners that
430 occupy bridge positions between functional modules, which could be the subject of future
431 investigations looking at the involvement of axo-axonic connections in precise behavior
432 modulation. Future opto-physiological experiments that probe those DNs will test whether
433 distributed control is the rule rather than the exception.
434
435 But what type of stimulus can activate the AN08B098 neurons? Anatomical evidence suggests
436 that upstream neurons can activate the AN08B098 neurons. Among them, the strongest inputs
437 come from: DNp103 (ACh), DNp06 (ACh), DNp59 (GABA) and IN12B015 (unknown).
438 Moreover, IN12B015 is activated by DNp05 (ACh) and DNp11 (ACh)[4]. Interestingly, DNp06
439 neurons contribute to long-mode takeoff, meanwhile DNp11 neurons evoke escape[35]. This
440 suggests that the same circuit that activates the GF and evokes the escape response also activates
441 the AN08B098 neurons, probably as a reinforcement mechanism to ensure efficacy in GF spiking.
442
443 Excitatory axo-axonic connections, like those we found in this paper (AN08B098 projecting
444 exclusively to GF), are also found in other animals, such as Mauthner cells in Zebrafish[36] and
445 Dopamine cells in mice[37]. In these examples, the main function of the excitatory axo-axonic
446 synapse is to increase the release probability of the axon terminal they innervate, and can even
447 bypass the action potentials generated upstream, a mechanism of hijacking that might have
448 physiological roles. We believe that the findings in this paper might contribute to the understanding
449 of the axo-axonic principles of connectivity in other animals.
450
451 One of the shortcomings of our work is that the connectome used in the analysis uses a single male
452 specimen; sex-specific or developmental differences remain to be evaluated once the Female Adult
453 Nerve Cord connectome (FANC) and late-larval volumes are released. All functional whole-

network tests are *in silico*, and although experimental verification is provided through optogenetics, the large-scale network of leaky integrate-and-fire neuron model respects synapse counts but ignores conductance dynamics and neuromodulators. Finally, EM of the MANC connectome (v1.2.1) did not detect gap-junctional coupling, so the present map under-reports electrical axo-axonic contacts that could further reshape information flow[38–42].

In conclusion, our study provides the first comprehensive blueprint of axo-axonic connectivity in a fully reconstructed adult nervous system. The sparse-yet-percolating architecture, chemistry-agnostic scaling, and distributed control we uncover offer concrete parameters for next-generation models of rapid motor decision making in both invertebrates and vertebrates. By formalizing how axons talk directly to axons, the work closes a major gap between connectome structure and motor function and opens new avenues for dissecting the fastest circuits in the animal kingdom.

Methods

Data acquisition and analysis

Data for VNC neurons used in the study came from the publicly available *Drosophila* male adult nerve cord connectome[4]. NeuPrint+ API[14,16] access is granted to registered users, and Python accessibility is maintained through the neuPrint-python package[15]. The latest *Drosophila* MANC data can be accessed here: https://www.janelia.org/project-team/flyem/manc-connectome.

Connectivity analysis

We retrieved all simple synaptic connections using neuprint.fetch_simple_connections[14–16] separately for: Outputs (AN, IN and DN as presynaptic) and Inputs (DN as postsynaptic). Connections were summed by partner neuron and filtered to those with total weight ≥ 6. For each DN, we then counted the number of distinct AN, IN, and DN partners in both the output and input directions.

Network analysis

Network analysis was performed using Python with the NetworkX[43] library to extract quantitative measures of connectivity. From the structural connectivity matrix, we calculated a comprehensive set of graph-theoretical metrics to characterize the network topology. These included basic properties (number of nodes and edges, network density), integration measures (average path length, diameter), segregation indices (clustering coefficient, modularity with community detection using the Louvain algorithm), centrality metrics (degree, betweenness, closeness, and eigenvector centrality), and organizational principles (degree assortativity, rich club coefficient).

The rich club analysis was specifically conducted across multiple degree thresholds to identify potential hierarchical organization among high-degree hub regions. All weighted graph measures incorporated the connection strengths from the original connectivity matrix. This multimodal graph-theoretical approach allowed for a detailed characterization of both local and global properties of the network's structural connectome, revealing important aspects of neural communication efficiency, functional segregation, and network resilience.

Statistical and visual analysis

SWC analysis was conducted in Python using the Navis client[44] . We stored morphology and input/output counts using Pandas. Relationships between morphology metrics (cable length, branch points, node count) and partner counts were assessed with Pearson correlation and linear regression (scipy.stats.pearsonr, linregress). Results were visualized with Matplotlib[45]. Network-style connection diagrams were rendered interactively with ipycytoscape.

Software and libraries

NeuPrint+ analyses were performed in Python 3.12.4 using the neuprint-python API. We used the Janelia NeuPrint client (neuprint), and Navis (v1.10.0) for data access and network building; data

manipulation and grouping were done with pandas v2.2.2 and NumPy v1.26.4; graph-based operations with NetworkX v3.2.1; interactive visualization with ipycytoscape v1.3.3 and ipywidgets v8.1.5; plotting and PDF export with Matplotlib v3.10.1; and statistical analyses (Pearson's r, linear regression) with SciPy[46] v1.13.1. Auxiliary parsing and utility functions relied on Python's built-in json, re, itertools, and warnings modules.

Computational model

To study the impact of axo-axonic projections onto DNp01 (GF), we constructed an *in-silico* model of the ventral nerve cord (VNC) by utilizing the entire MANC v1.2.1 connectome. First, we scrubbed the connectivity data by omitting connections with a total weight less than 6, then we excluded all connectivity data where the neurotransmitter type, neuron type, or neuron ID was unknown or invalid. This resulted in a total of 23,437 valid neurons and 1,152,548 connections between them, 619,684 of which were excitatory (cholinergic), and 532,864 of which were inhibitory (glutamatergic or GABAergic). In the fly, cholinergic receptors are excitatory, meanwhile glutamatergic and GABAergic receptors are inhibitory[47].

Neuron model

To achieve biological plausibility while avoiding computational intractability, leaky integrate-and-fire (LIF) neuron models were used:

$$C_m \frac{dv}{dt} = -g_L(v - V_{rest}) - g_{ach}(v - E_{ach}) - g_{gaba}(v - E_{gaba}) - g_{glut}(v - E_{glut}), \quad (1)$$

Where v is the neuron membrane potential, g_L, g_{ach}, g_{GABA}, and g_{glut} are the conductances for leak channels and acetylcholine (nicotinic), GABA ($GABA_A$), and glutamate ionotropic receptors (nAChR, $GABA_AR$, and GluCl, respectively). Similarly, V_{rest}, E_{ach}, E_{GABA}, and E_{glut} are their respective reversal potentials. Since $GABA_AR$ and GluR are chloride-permeable channels, their reversal potentials were obtained from chloride reversal potential[48]. C_m is the membrane capacitance. These are parameterized with values found from literature investigating the biophysical properties of fruit fly synapses. Furthermore, we collected physiologically relevant values for the membrane capacitance, resistance, and leak reversal potential**.** Simulations of these neurons were made using the BRIAN2 simulator[49].

Synapse model

For each of the synaptic currents ($x = ach, gaba, glut$), the conductance obeys

$$\frac{dg_x}{\tau_x} = -g_x, \quad (2)$$

which increases by J_x upon a presynaptic spike. The list of parameters is included in Table 1.

Parameter	Symbol	Value	Ref.
Acetylcholine receptor (nAChR) conductance	J_{ach}	0.27 nS	[50]
nAChR decay time	τ_{ach}	1.1 ms	[50]
nAChR reversal potential	E_{ach}	0 mV	[51]
GABA receptor ($GABA_AR$) conductance	J_{GABA}	0.8 nS	Estimated
$GABA_AR$ decay time	τ_{GABA}	5.4 ms	[52]
$GABA_AR$ reversal potential	E_{GABA}	-60 mV	[47,48]
Glutamate receptor (GluCl) conductance	J_{glut}	0.8 nS	Estimated
GluCl decay time	τ_{glut}	5 ms	[53]
GluCl reversal potential	E_{glut}	-60 mV	[48]
Membrane Resistance	R_m	300 MOhm	[54]
Resting membrane potential	V_{rest}	-55 mV	[54]
Action potential threshold	V_{th}	-40 mV	[54]
Reset potential	V_{reset}	-55 mV	Estimated
Refractory period	τ_{ref}	2 ms	Estimated
Membrane capacitance	C_m	72 pF	[54]

Table 1. List of parameters used in the connectome simulation of the VNC in this paper. For each of our simulations, we ran the entire VNC network with a step-size of 0.1 ms during 2000 ms. Furthermore, for each simulation, each neuron in the VNC network was provided with an excitatory Poisson input of 30 Hz at a weight of 5 nS to simulate typical endogenous activity driven by neurons in the fly brain. During stimulation experiments, neurons DNp01, DNg02, and/or DNd03 were stimulated with additional Poisson input at 10 Hz at a weight of 40 nS. In Figure 8, the same network was used, but the GF was electrically stimulated just below threshold with a Poisson-distributed stimulation at 24 Hz.

Fly Genetics

Flies were raised at 25°C with a natural (12-hr) light cycle, and data were collected from both male and female adults 2-4 days old. The Gal4 drivers used in our study were selected through NeuronBridge[55]. Briefly, neurons of interest were identified through neuPrint+, then identified using NeuronBridge software v3.2.6 and chosen based on similarity score and visual accuracy. A split-Gal4 driver specific to AN08B098 was identified using NeuronBridge software v3.2.6 and chosen based on similarity score. SS25451 contains Andorra-p65(AD)::Zip+/+; c12.1-Gal4(DBD)::Zip-/- (BDSC #89495). Constructs used were UAS-csChrimson-mVenus (#55136), and P{20XUAS-IVS-mCD8::GFP}attP2 (BDSC #32194).

561 **Electrophysiology**
562 Flies were placed dorsal side up in dental wax after CO_2 anesthesia. Muscle recordings were
563 obtained using glass microelectrodes placed directly into both left and right tergotrochanteral jump
564 muscles[8,17,39,42,56] (TTM). Microelectrodes were filled with O'Dowd's Drosophila saline[57].
565 Stimulation of the Giant Fibers was done using 3-4 V applied extracellularly using Grass
566 stimulators with tungsten wire electrodes placed in the brain through the eyes, and a tungsten wire
567 electrode was placed in the fly's abdomen to ground the circuit[17]. The Axon Digidata 1440A Data
568 Acquisition System was used to digitize recordings which are then visualized using Clampex
569 software (version 10 & 11, Molecular Devices). Muscle responses were obtained by stimulating
570 at 24 Hz.
571
572 **Optogenetics**
573 We drove channelrhodopsin expression in neurons of interest using the UAS-Gal4 system. Flies
574 expressing csChrimson (BDSC #55136) were crossed with our driver lines to produce: w1118;
575 VT063643/+; 20XUAS-IVS-csChrimson.mVenus/VT059224-GAL4. Adults were placed in the
576 dark at 50% relative humidity on standard cornmeal-molasses food, supplemented with all-trans-
577 retinal (0.4 mM post-eclosion) for two days before testing. Light stimulation was performed for
578 100 ms while flies are mounted in dental wax as described above. We used a 590 nm high-power
579 fiber-coupled LED (1.5 mW maximum light intensity, Thorlabs M590F3) with an optic fiber of
580 diameter 200 µm and N.A. 0.22 to activate the mVenus csChrimson (M118L02). We tested various
581 placements for the optic fiber and found the strongest activation of csChrimson to occur when the
582 fiber was less than 1 cm from the sample and aimed at the neck. Light intensity was controlled via
583 T-Cube LED Driver (Thorlabs LEDD1B) and kept at maximum power during testing. Each sample
584 received electrical-only, optogenetic-only or paired opto-electrical stimulation.
585
586 We also ran two control experiments for the optogenetic protocol (Fig. *S*2). The first control used
587 flies of the same genotype as the experimental flies above, and were not raised on food
588 supplemented with all-trans-retinal. The second control uses flies raised on food supplemented
589 with all-trans-retinal but genetically lack UAS-csChrimson.mVenus (w1118; VT063643/+;
590 VT059224-GAL4/VT059224-GAL4). The results are shown in Figure *S*2.
591
592 **Dye-injection**
593 The VNC and connective of young adult male flies were dissected and kept in cold O'Dowd's
594 saline within a Sylgard 184-filled dissection dish. Samples were immediately transferred to a
595 Nikon Eclipse E600FN fluorescent microscope. A tetramethylrhodamine-labeled dextran dye
596 (10,000MW, Invitrogen, D1817) solution was backfilled into a pulled glass electrode tip (~30 MΩ
597 resistance tip) and filled with O'Dowd's saline. Electrodes were placed into a 3D hydraulic
598 micromanipulator. The electrode was lowered into place, penetrating the GF axons near the neck
599 connective. A Gettings Model 5A amplifier was used to inject positive current pulses (between 1

nA and 5 nA), with a reference electrode placed into the saline-filled dish. GFs were filled with dye for approximately 5 minutes each.

Immunostaining

A mouse primary antibody against ChAT (1:20, DSHB, 4B1) was used to confirm cholinergic cells and coupled to secondary Goat anti-mouse AlexaFluor 647 (1:500, 115-605-003). A mouse primary antibody against bruchpilot (1:50, DSHB, NC82) was used to labeled presynaptic chemical active zones and coupled to secondary Goat anti-mouse AlexaFluor 647 (1:500, 115-605-003). Primary rabbit anti-GFP (1:500, Invitrogen A11122) and secondary goat anti-rabbit (1:500, Jackson Immuno, 111-225-144) were used to amplify the fluorescence of mCD8::GFP. mVenus-tagged csChrimson fluorescence was amplified using a conjugated antibody (1:500, Millipore, MABE1906). Primary antibody solutions contained 3% BSA and 0.3% Triton X-100 in PBS. The secondary antibody solutions were PBS.

Samples were dissected and processed according to the dye-injection methods above. Samples were then immediately fixed in PBS + 4% PFA for 25 minutes at room temperature (22°C). Samples were washed with PBS and placed on a rotator (60RPM) for 30 minutes. Samples were permeabilized with PBS + 0.5% Triton X-100 for 45 minutes at 22°C. Primary antibodies were added, and samples were stored at 4°C for 48 hours. Samples were then washed on a rotator with PBS for 4 hours at 22°C, changing the solution every 30 minutes. Secondary antibodies were added, and samples were stored at 4°C for 24 hours. Samples were then washed on a rotator with PBS for 4 hours at 22°C, changing the solution every 30 minutes. Samples were dehydrated with a series of ethanol steps, 50%, 70%, 90%, and 100% for 8 minutes each step. Samples were trimmed and embedded in 100% methylsalycylate, covered with cover slips, sealed, and imaged within 24 hours.

Confocal Microscopy

Samples were imaged on a Nikon AXR confocal using an NSPARC detector and a 60x oil immersion objective. Z-dimension step size was 194 μm for all results displayed. Laser channels used were 488 nm, 561 nm, and 640 nm. Channels were imaged in series using filters to avoid cross-excitation of close wavelengths, and 2x integration was used.

Image Analysis

Z-stack files were imported into Imaris software v10.2.0, and the fluorescence intensity of each channel was adjusted for best fit. GF and AN08B098 channels were surfaced using a thresholding method that matched fluorescence in each Z dimension. Masks of each channel were created for each surface to detect colocalization of Brp or ChAT. Images were acquired in volume view and exported.

Acknowledgments

R.P. was funded by an IBRO Collaborative Research Grants. The authors thank the FAU Jupiter Life Sciences Initiative (JLSI) for funding.

Author contributions

C.C.C. and R.P. were responsible for the conceptualization of the work. C.C.C., J.L., T.R., D.S., S.J., and C.S. analyzed the data and made the figures. R.P. worked on the graph theoretical measures. D.S. performed and analyzed the electrophysiology recordings. S.J. and C.S. performed immunofluorescence. K.R. maintained fly stocks. T.R. built and ran the network simulations. R.P., C.S., and R.M. supervised the research and secured funding. All authors participated in the writing, reviewed, and approved the manuscript.

Competing interests

The authors declare no competing interests.

References

1. Schneider-Mizell, C. M. *et al.* Structure and function of axo-axonic inhibition. *Elife* **10**, (2021).
2. Brette, R. Theory of axo-axonic inhibition. *PLoS Comput Biol* **21**, e1013047 (2025).
3. Takemura, S.-Y. *et al.* A Connectome of the Male *Drosophila* Ventral Nerve Cord. *bioRxiv* (2023).
4. Cheong, H. S. J. *et al.* Transforming descending input into behavior: The organization of premotor circuits in the Drosophila Male Adult Nerve Cord connectome. *bioRxiv* (2023).
5. Marin, E. C. *et al.* Systematic annotation of a complete adult male Drosophila nerve cord connectome reveals principles of functional organisation. *Elife* **13**, (2024).
6. Lin, A. *et al.* Network statistics of the whole-brain connectome of Drosophila. *Nature 2024 634:8032* **634**, 153–165 (2024).
7. Clements, J. *et al.* neuPrint: Analysis Tools for EM Connectomics. *bioRxiv* 2020.01.16.909465 (2020) doi:10.1101/2020.01.16.909465.
8. Allen, M. J., Godenschwege, T. A., Tanouye, M. A. & Phelan, P. Making an escape: Development and function of the Drosophila giant fibre system. *Seminars in Cell and Developmental Biology* vol. 17 Preprint at https://doi.org/10.1016/j.semcdb.2005.11.011 (2006).
9. Asinof, S. K. & Card, G. M. Neural Control of Naturalistic Behavior Choices. *Annu Rev Neurosci* **47**, 369–388 (2024).
10. Cheong, H. S. J. *et al.* Transforming descending input into behavior: The organization of premotor circuits in the Drosophila Male Adult Nerve Cord connectome. *bioRxiv* (2023).
11. Stürner, T. *et al.* Comparative connectomics of Drosophila descending and ascending neurons. *Nature 2025* 1–15 (2025) doi:10.1038/s41586-025-08925-z.
12. Takemura, S. *et al.* A Connectome of the Male Drosophila Ventral Nerve Cord. *Elife* **13**, (2024).
13. Marin, E. C. *et al.* Systematic annotation of a complete adult male Drosophila nerve cord connectome reveals principles of functional organisation. *Elife* **13**, (2024).
14. Plaza, S. M. *et al.* neuPrint: An open access tool for EM connectomics. *Front Neuroinform* **16**, (2022).
15. Berg, S. & Schlegel, P. neuprint-python. Preprint at https://doi.org/10.5281/zenodo.7592899 (2017).
16. Clements, J. *et al.* neuPrint: Analysis Tools for EM Connectomics. *bioRxiv* 2020.01.16.909465-2020.01.16.909465 (2020) doi:10.1101/2020.01.16.909465.
17. Allen, M. J. & Godenschwege, T. A. Electrophysiological recordings from the Drosophila giant fiber system (GFS). *Cold Spring Harb Protoc* **5**, (2010).
18. Klapoetke, N. C. *et al.* Independent optical excitation of distinct neural populations. *Nat Methods* **11**, (2014).
19. Scheffer, L. K. *et al.* A connectome and analysis of the adult drosophila central brain. *Elife* **9**, (2020).
20. Manoim, J. E., Davidson, A. M., Weiss, S., Hige, T. & Parnas, M. Lateral axonal modulation is required for stimulus-specific olfactory conditioning in Drosophila. *Current Biology* **32**, 4438-4450.e5 (2022).
21. Gruber, L. *et al.* The unique synaptic circuitry of specialized olfactory glomeruli in Drosophila melanogaster. Preprint at https://doi.org/10.7554/eLife.88824.1 (2023).

22. Calle-Schuler, S. A., Santana-Cruz, A. E., Kmecová, L., Hampel, S. & Seeds, A. M. A comprehensive mechanosensory connectome reveals a somatotopically organized neural circuit architecture controlling stimulus-aimed grooming of the *Drosophila* head. Preprint at https://doi.org/10.1101/2025.05.19.654894 (2025).
23. Oleskevich, S., Descarries, L., Watkins, K. C., Se´gue´la, P. & Daszuta, A. Ultrastructural features of the serotonin innervation in adult rat hippocampus: An immunocytochemical description in single and serial thin sections. *Neuroscience* **42**, 777–791 (1991).
24. Cover, K. K. & Mathur, B. N. Axo-axonic synapses: Diversity in neural circuit function. *Journal of Comparative Neurology* **529**, 2391–2401 (2021).
25. Séguéla, P., Watkins, K. C. & Descarries, L. Ultrastructural relationships of serotonin axon terminals in the cerebral cortex of the adult rat. *Journal of Comparative Neurology* **289**, 129–142 (1989).
26. Lin, A. *et al.* Network statistics of the whole-brain connectome of Drosophila. *Nature 2024 634:8032* **634**, 153–165 (2024).
27. Lu, J. *et al.* Selective inhibitory control of pyramidal neuron ensembles and cortical subnetworks by chandelier cells. *Nat Neurosci* **20**, (2017).
28. Woodruff, A. R., Anderson, S. A. & Yuste, R. The Enigmatic Function of Chandelier Cells. *Front Neurosci* **4**, (2010).
29. Cuntz, H., Forstner, F., Borst, A. & Häusser, M. One rule to grow them all: A general theory of neuronal branching and its practical application. *PLoS Comput Biol* **6**, (2010).
30. Lacin, H. & Truman, J. W. Lineage mapping identifies molecular and architectural similarities between the larval and adult Drosophila central nervous system. *Elife* **5**, (2016).
31. Rajagopalan, S., Nicolas, E., Vivancos, V., Berger, J. & Dickson, B. J. Crossing the midline: Roles and regulation of Robo receptors. *Neuron* **28**, (2000).
32. Harriger, L., van den Heuvel, M. P. & Sporns, O. Rich Club Organization of Macaque Cerebral Cortex and Its Role in Network Communication. *PLoS One* **7**, e46497 (2012).
33. Liang, X. *et al.* The Rich-Club Organization in Rat Functional Brain Network to Balance Between Communication Cost and Efficiency. *Cerebral Cortex* **28**, 924–935 (2018).
34. Card, G. & Dickinson, M. H. Visually Mediated Motor Planning in the Escape Response of Drosophila. *Current Biology* **18**, (2008).
35. Dombrovski, M. *et al.* Synaptic gradients transform object location to action. *Nature* **613**, (2023).
36. Lacoste, A. M. B. *et al.* A Convergent and Essential Interneuron Pathway for Mauthner-Cell-Mediated Escapes. *Current Biology* **25**, 1526–1534 (2015).
37. Kramer, P. F. *et al.* Synaptic-like axo-axonal transmission from striatal cholinergic interneurons onto dopaminergic fibers. *Neuron* **110**, 2949-2960.e4 (2022).
38. Ammer, G., Vieira, R. M., Fendl, S. & Borst, A. Anatomical distribution and functional roles of electrical synapses in Drosophila. *Current Biology* **32**, (2022).
39. Lopez, J., Boerner, J., Robbins, K., Pena, R. F. O. & Murphey, R. Frazzled/DCC regulates gap junction formation at a Drosophila giant synapse through transcription. Preprint at https://doi.org/10.1101/2025.04.08.647628 (2025).
40. Holcroft, C. E. *et al.* Innexins Ogre and Inx2 are required in glial cells for normal postembryonic development of the Drosophila central nervous system. *J Cell Sci* **126**, 3823–3834 (2013).

41. Phelan, P. *et al.* Molecular mechanism of rectification at identified electrical synapses in the Drosophila giant fiber system. *Curr Biol* **18**, 1955–1960 (2008).
42. Orr, B. O., Borgen, M. A., Caruccio, P. M. & Murphey, R. K. Netrin and frazzled regulate presynaptic gap junctions at a Drosophila giant synapse. *Journal of Neuroscience* **34**, (2014).
43. Hagberg, A. A., Schult, D. A. & Swart, P. J. Exploring Network Structure, Dynamics, and Function using NetworkX. in *Proceedings of the 7th Python in Science Conference* (2008). doi:10.25080/tcwv9851.
44. Schlegel, P. *et al.* navis-org/navis: Version 1.10.0. Preprint at (2025).
45. Hunter, J. D. Matplotlib: A 2D graphics environment. *Comput Sci Eng* **9**, (2007).
46. Virtanen, P. *et al.* SciPy 1.0: fundamental algorithms for scientific computing in Python. *Nat Methods* **17**, (2020).
47. McCarthy, E. V *et al.* Synchronized bilateral synaptic inputs to Drosophila melanogaster neuropeptidergic rest/arousal neurons. *Journal of Neuroscience* **31**, (2011).
48. Schnizler, K. *et al.* A novel chloride channel in Drosophila melanogaster is inhibited by protons. *Journal of Biological Chemistry* **280**, (2005).
49. Stimberg, M., Brette, R. & Goodman, D. F. M. Brian 2, an intuitive and efficient neural simulator. *Elife* **8**, (2019).
50. Moreno-Sanchez, A. *et al.* Morphology and synapse topography optimize linear encoding of synapse numbers in Drosophila looming responsive descending neurons. Preprint at https://doi.org/10.7554/eLife.99277.1 (2024).
51. Lee, D. & O'Dowd, D. K. Fast excitatory synaptic transmission mediated by nicotinic acetylcholine receptors in Drosophila neurons. *Journal of Neuroscience* **19**, (1999).
52. Lee, D., Su, H. & O'Dowd, D. K. GABA receptors containing Rdl subunits mediate fast inhibitory synaptic transmission in Drosophila neurons. *Journal of Neuroscience* **23**, (2003).
53. Saumweber, T. *et al.* Behavioral and synaptic plasticity are impaired upon lack of the synaptic protein SAP47. *Journal of Neuroscience* **31**, (2011).
54. Churgin, M. A. *et al.* A neural correlate of individual odor preference in Drosophila. *Elife* **12**, (2025).
55. Clements, J. *et al.* NeuronBridge: an intuitive web application for neuronal morphology search across large data sets. *BMC Bioinformatics* **25**, (2024).
56. Augustin, H. *et al.* Reduced insulin signaling maintains electrical transmission in a neural circuit in aging flies. *PLoS Biol* **15**, e2001655–e2001655 (2017).
57. Gu, H. & O'Dowd, D. K. Cholinergic Synaptic Transmission in Adult Drosophila Kenyon Cells In Situ. *Journal of Neuroscience* **26**, 265–272 (2006).

789
790
791
792
793
794
795
796
797
798
799
800 **Supplementary Material**
801

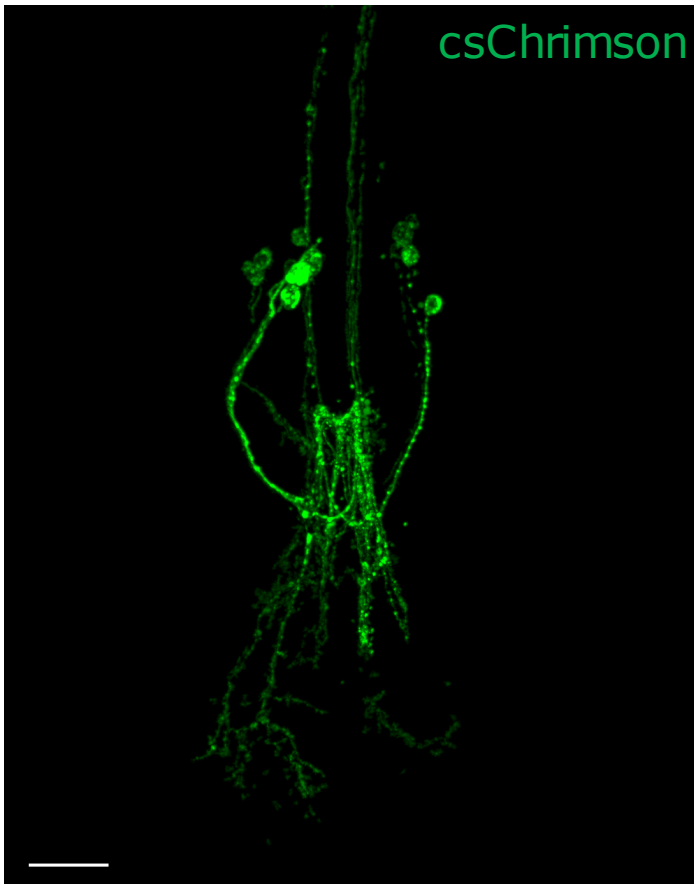

802
803 **Figure S1.** Immunofluorescence of mVenus-tagged csChrimson. csChrimson was expressed along the axons and
804 within the somas of the AN08B098 population. Scale bar represents 5 mm.
805

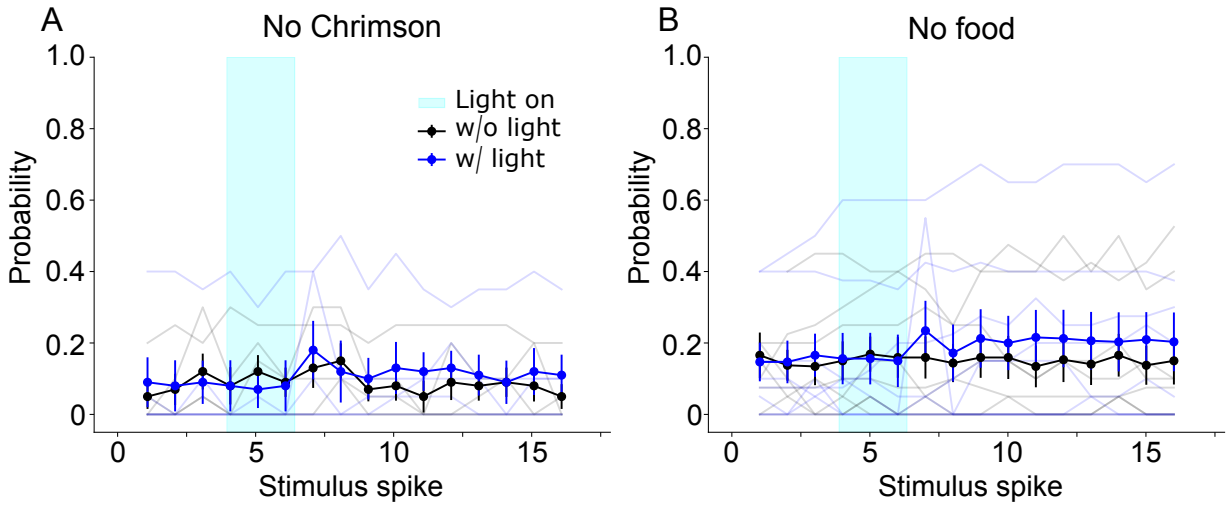

Figure S2. Control experiments for the optogenetics protocol. (*A*) Electrical recordings from the jump muscle of flies lacking Chrimson expression (n = 5 flies). (*B*) Electrical recordings from the jump muscle of flies expressing Chrimson in AN08B098 neurons but not provided with food supplemented with all-trans-retinal (n = 8 flies). No significant differences were observed between treatment groups.